Endogenous Osteocyte-Osteoclast Signaling Enables Growth Factor-Free Bone Remodeling, Drug Response, and Cancer Invasion in a Nanoscale Calcified Bone-on-a-Chip Model

Mauricio G.C. Sousa[1,6] #, Avathamsa Athirasala[1,6] #, Daniela M. Roth[1,6], May Anny A. Fraga[7], Sofia M. Vignolo[1,3,5], Aaron Doe[2], Jinho Lee[8], Genevieve E. Romanowicz[9], Jonathan V. Nguyen[6], Angela S.P. Lin[7], Cristiane M. Franca[1,6], Robert E. Guldberg[9], Luiz E. Bertassoni[1,3,4,5,6]

[1] Knight Cancer Precision Biofabrication Hub, Cancer Early Detection Advanced Research (CEDAR), Knight Cancer Institute, Oregon Health & Science University, Portland, Oregon, USA.

[2]Cancer Early Detection Advanced Research (CEDAR), Knight Cancer Institute, Oregon Health & Science University, Portland, Oregon, USA.

[3] Division of Oncological Sciences, Knight Cancer Institute, Oregon Health & Science University, Portland, Oregon, USA.

[4] Center for Regenerative Medicine, School of Medicine, Oregon Health & Science University, Portland, Oregon, USA.

[5] Department of Biomedical Engineering, School of Medicine, Oregon Health & Science University, Portland, Oregon, USA.

[6] Department of Oral Rehabilitation and Biosciences, School of Dentistry, Oregon Health & Science University, Portland, Oregon, USA.

[7] Department of Restorative Dentistry, Faculdade de Odontologia de Piracicaba (FOP), Universidade Estadual de Campinas, Piracicaba, São Paulo, Brazil.

[8] Precision oncology, Knight Cancer Institute, Oregon Health and Science University, Portland, Oregon, USA.

[9] Knight Campus for Accelerating Scientific Impact, University of Oregon, Eugene, Oregon, USA.

Corresponding author:

Luiz E. Bertassoni

Email: bertasso@ohsu.edu

# Equal contribution.

Abstract

Bone homeostasis depends on spatially orchestrated interactions among osteoclasts, osteoblasts, and osteocytes that are embedded within a unique extracellular matrix that is mineralized on the nanoscale to define the structure and function of bone. Reconstructing these interactions to enable autonomous cell differentiation and tissue remodeling has remained a significant challenge towards mimicking adequate bone physiology in-vitro. Here, we present an engineered model that spatially defines the paracrine communication of heterogeneous cell populations within bone tissue that support the rapid maturation of primary osteoblasts into osteocytes, the differentiation of macrophages into osteoclasts, and calcified tissue resorption within a mineralized cell-laden bone-like tissue. We demonstrate that nanoscale mineralization of cell-laden collagen hydrogels on-a-chip enhances osteoblast to osteocyte differentiation, whereas osteocytes in the matrix accelerate osteoclastogenesis and remodeling in a spatially defined manner without the need for exogenous growth factors. Osteocyte-dependent osteoclastogenesis on-a-chip outperformed conventional stimulation with RANKL and M-CSF, reproduced the clinical response of anti-resorptive drugs, and mimicked established tumor-bone interactions observed in invasive oral cancer. By replicating essential aspects of bone composition and function, this system provides a robust, self-regulated microphysiologic model to investigate bone remodeling, cancer-bone crosstalk, and therapeutic interventions.

Keywords: bone-on-a-chip, osteocytes, osteoclastogenesis, biomimetic bone

1. Main

Bone-related diseases, including fractures, cancers, and osteoporosis, impose a global economic burden projected to exceed $25 billion in 2025[1, 2, 3, 4]. Despite the growing demand for effective bone treatments, existing preclinical models fall short in capturing the complex and dynamic interplay between the cellular machinery and structural components of bone, thus considerably limiting our ability to unravel the mechanisms that govern bone homeostasis, remodeling, and disease[5, 6]. Bone is a dynamic organ system whose formation and homeostasis depend on a tightly orchestrated sequence of cell-cell and cell-matrix interactions occurring within a highly specialized microenvironment.[7, 8, 9] In its mature form, bone is composed of a densely mineralized collagen matrix that embeds cells in three dimensions (3D), forming a stiff, hierarchically organized tissue capable of sensing, adapting to, and remodeling in response to physiological demands.[10, 11, 12] This mineralization arises through a nanoscale process in which calcium and phosphate ions are precisely guided into collagen fibrils by matrix-regulating proteins, resulting in the formation of intrafibrillar hydroxyapatite crystals[13, 14, 15]. These nanoscale mineralized collagen fibrils define the architecture and mechanical stiffness of the matrix and, critically, establish the cell-binding and ionic domains that regulate cell behavior[16, 17, 18, 19, 20]. For example, it has been demonstrated that cells sense and respond to this mineralized environment through mechanotransductive and ion-mediated signaling pathways that are essential for osteoblast differentiation and osteocyte function[21, 22, 23]. Embedded in the matrix, osteocytes act as central regulators of bone remodeling. They secrete paracrine cues that modulate both osteoblast activity and the recruitment and differentiation of osteoclast precursors[24, 25]. Through this mechanism, osteocytes control the remodeling events that occur in bone tissue, including those involved in resorption, adaptation, and pathologic bone loss[26, 27, 28]. Engineering a human-relevant system that faithfully reproduces these dynamic and endogenously regulated cell-cell and cell-matrix interactions represents not only a complex challenge but a critical need.

Current in-vitro models fail to recapitulate many of the essential hallmarks of bone, including chemical, physical, and biological features[29]. Most rely on non-mineralized collagen matrices that lack the biochemical complexity and mechanical cues of the native nanoscale-

calcified bone matrix. Alternatives such as hydroxyapatite-coated plates, bone explants, and demineralized bone surfaces, though considered gold standards for studying bone resorption, replicate some of the properties of native bone while neglecting the complex interplay of cell-cell and cell-matrix communication that is known to result in a self-regulating remodeling unit that defines bone physiology[30, 31, 32]. For example, osteoclastogenesis in these models is typically induced through supraphysiologic supplementation with recombinant receptor activator of nuclear factor κB ligand (RANKL) and macrophage colony-stimulating factor (M-CSF), thereby bypassing the natural signaling hierarchy regulated by the communication between osteocytes, osteoblasts, and osteoclasts[33, 34]. Even advanced 3D and organ-on-a-chip platforms often feature osteoblasts on soft or non-calcified matrices and fail to recapitulate the spatial architecture of entrapped osteocytes in intrafibrillar mineralized collagen fibers or the paracrine loops that define the regulation of bone turnover[35, 36]. These limitations compromise the ability of current models to reproduce the temporal sequence of events that drive bone adaptation,and resorption. Therefore, the relevance of existing engineered bone models to study drug response, pathophysiology, or cell-matrix interactions at the bone surface is limited. An autonomous microphysiological system that mimics established hallmarks of bone physiology - where a nanostructurally mineralized collagen matrix osteoblast to osteocyte differentiation, and osteocytes coordinate the activity of osteoclasts and osteoblasts - remains an unmet need in translational bone research.

To address these gaps, here we introduce a bone-on-a-chip platform that spatially organizes human osteoblasts, osteocytes, macrophages, osteoclasts, and endothelial cells within a nanostructured mineralized matrix, enabling the temporally-controlled cell state transitions that are essential for bone remodeling and self-regulation. Unlike conventional models, this microphysiological system supports terminal osteogenic differentiation and functional osteoclastogenesis through endogenous cell-cell and cell-matrix communication without the need for exogenous supplements and growth factors. Moreover, this self-regulated system allows for osteoclast differentiation events via physiologic pathways that are different from those observed with standard M-CSF- and RANKL-supplemented differentiation medium. The resulting system exhibits robust resorptive behavior observed via micro-CT, responds to clinical-grade anti-resorptive drugs, and mimics the invasion of oral squamous cell carcinoma (OSCC) into bone by recapitulating bone reportion in the progression of oral cancer. In summary, this biomimetic

bone-on-a-chip platform addresses critical gaps in existing models by authentically replicating the complex microenvironment of bone. This provides a novel and robust, physiologically relevant tool to study bone homeostasis, disease mechanisms, and therapeutic responses in-vitro for preclinical research in bone-targeting diseases and therapeutic interventions.

2. Results

2.1. Bone-like nanostructure supports osteocyte differentiation without osteoinductive supplements

Bone is a hierarchical structure organized at the nanoscale level by mineralized collagen fibers, which are critical for osteocyte differentiation and the regulation of osteoclastogenic factors[37]. To replicate this nanostructure in-vitro, we developed a biomimetic model by embedding osteoblasts in a collagen matrix (2.5 mg/mL) within a microfluidic device featuring a central channel flanked by two lateral channels that can be independently perfused. The osteoblast-laden collagen matrix was injected into the main channel and underwent mineralization over a 3-day period. We followed a previously developed strategy to achieve mineralization using previously optimized media containing physiological levels of calcium (Ca^{2+}), phosphate (PO_4^{3-}), and a matrix protein analogue (Lacprodan mOPN-10). This media composition delays premature precipitation of the calcium and phosphate in solution, allowing amorphous calcium phosphate to penetrate individual collagen fibrils and nucleate intrafibrillarly, mimicking native bone mineralization as demonstrated in previous studies[38, 39]. This process not only mimics the microarchitecture and composition of bone tissue (Fig.1a) but also supports the presence and function of key resident bone cells (osteoblasts, osteoclasts, and osteocytes) within a spatially organized platform (Fig. 1a-b). We first confirmed the ability of the model to induce nanoscale mineralization compared to non-mineralized control samples (NM). Scanning electron microscopy (SEM) analysis (Fig. 1c-d) revealed significant differences in fiber structure between the groups, with mineralized samples (MIN) illustrating distinct mineral deposits on the collagen fibers. These fiber structural changes were absent in non-mineralized samples (Fig. 1c). Additionally, the mineralization process was confirmed using alizarin red staining, which demonstrated visible mineral deposition in the mineralized groups

(Supplementary Fig. 1a-d). Fourier Transform Infrared Spectroscopy (FTIR) was performed further to confirm the chemical composition of the mineralized matrix. The mineralized samples exhibited prominent peaks corresponding to expected apatite phosphate (1030, 600, and 560 cm^{-1}), carbonate (874 cm^{-1}), and amide bands (1649, 1553, and 1248 cm^{-1}), absent in the non-mineralized controls (Fig. 1e). These findings align with patterns observed in native bone[38, 39, 40]. Quantitative analyses showed significantly higher mineral-to-matrix ratios and crystallinity indexes in mineralized samples compared to controls, and comparable mineralization relative to native bone[40], corroborating the ability of this model to replicate key properties of bone tissue at the nanoscale level.

In the physiological context of bone, osteoblasts secrete a dense collagenous matrix, termed osteoid, which eventually mineralizes to entrap the cells, triggering their transition into osteocytes[41]. To determine whether the mineralized matrix in our system supports this transition, we first confirmed that the mineralized matrix did not affect the viability of human osteoblasts over the 3-day mineralization process (Supplementary Fig. 2). Samples were then fixed and immunostained to assess the morphological structure of osteocyte differentiation. In the mineralized groups, cells exhibited pronounced morphological changes consistent with osteocyte maturation, including significantly elongated cytoplasmic processes, higher aspect ratios, and the emergence of dendritic extensions; all features that are consistent with a more mature osteocyte network phenotype **(**Fig. 2a-b and Supplementary Figs. 3 and 4). In contrast, cells in the non-mineralized groups retained the rounded morphology typical of undifferentiated osteoblasts. Furthermore, the expression of podoplanin (PDPN) was visible in osteocyte connections (Figure 1h-i and Supplementary Figure 4a-b), and sclerostin (SOST) expression higher in mineralized samples, which is consistent with the mechanically stiff, mineralized microenvironment and the known upregulation of this marker during terminal osteocyte differentiation, as observed in bone[37, 42]. Collectively, the elongation of the osteoblasts, the formation of dendritic extensions, and the upregulation of mechanosensitive PDPN and SOST align with the phenotypic transition from osteoblasts to osteocytes[43, 44]. When compared with treatment with classic osteoinductive media for seven days, the expression of PDPN was not significantly different between mineralized and osteoinductive samples, showing that our model stimulates faster osteocyte differentiation without the use of osteoinductive media (Supplementary Fig. 5). Our platform's nanoscale mineralized matrix promotes osteoblast-to-osteocyte transition through spatial

confinement and pericellular stiffness, accompanied by increased production of mechanosensitive proteins, even without the use of traditional exogenous osteoinductive factors[45]. The regulation of osteocyte differentiation in a significantly accelerated timeline represents an important step to provide the mechanical and cellular cues to prepare a bone-prototypical environment for remodeling.

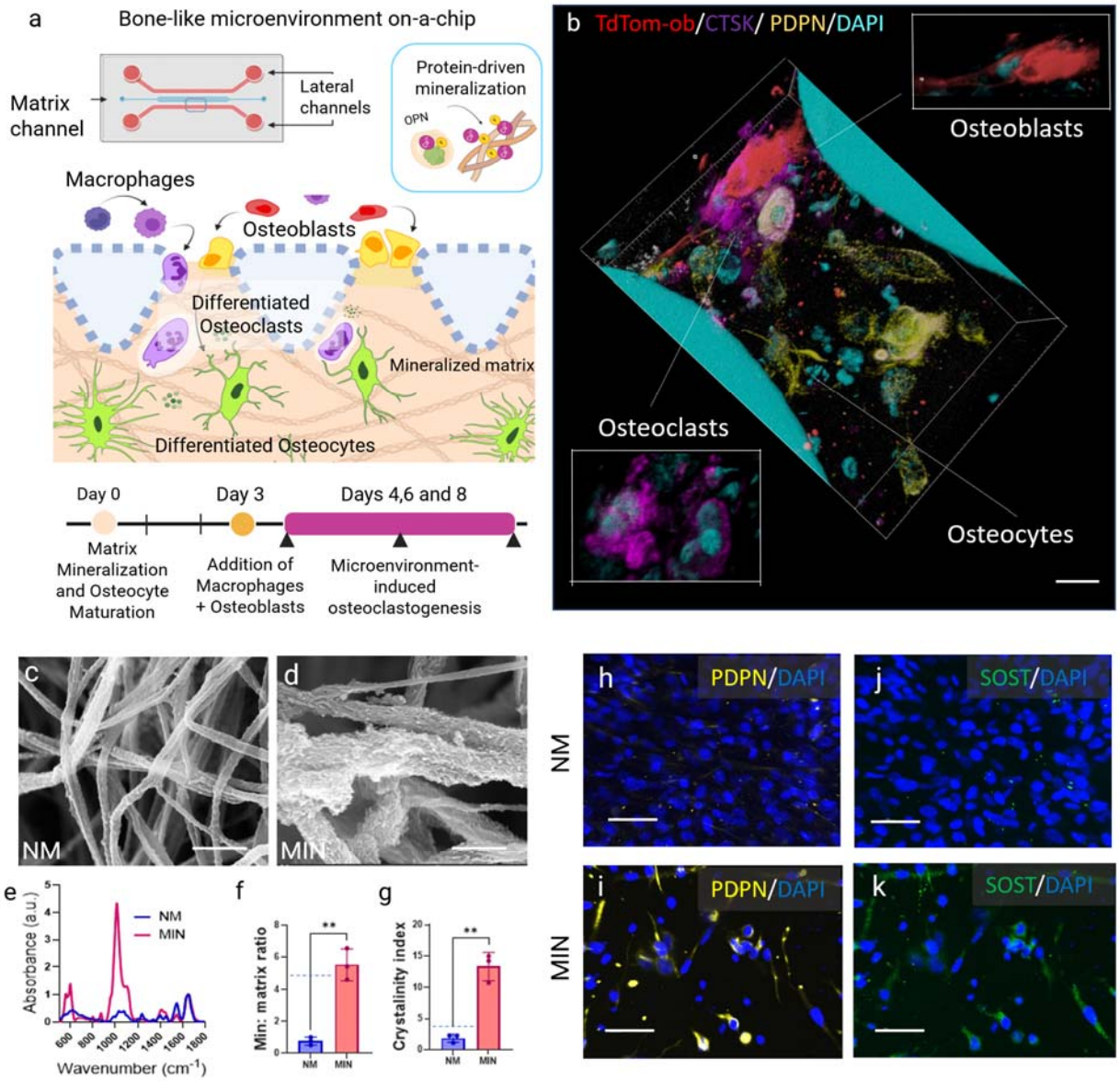

Figure 1. Bone-on-a-chip recapitulates the self-regulating multicellular complexity of bone within a mineralized matrix. *(a) Conceptual schematic illustrating bone cells embedded within a mineralized microenvironment to form a bone-like interface using an organ-on-a-chip platform that recapitulates key physiological interactions occurring in vivo. (b) The engineered system enables the co-existence and direct interaction of osteoblasts, osteocytes, macrophages, and osteoclasts without the need for exogenous differentiation factors. Osteoblasts embedded within a collagen matrix undergo mineralization-driven differentiation into osteocytes (podoplanin, PDPN; yellow). After mineralization, macrophages naturally differentiate into osteoclasts (cathepsin K, CTSK; magenta) and tdTom-osteoblasts (tdTom-ob; red) are introduced at the bone interface, allowing physiologically relevant, growth factor–independent crosstalk among these cell types. This coordinated cascade establishes an autonomous, self-regulating bone-like microenvironment within a mineralized extracellular matrix. The SEM images (c-d) show the formation of*

*fibril bundles and apparent extra-fibrillar mineral deposition in mineralized samples (MIN) when compared to non-mineralized groups (NM). FTIR spectra (e) and respective mineral: matrix ratio (f) and (g) crystallinity index illustrate significantly higher mineral composition in mineralized groups. (h-k) illustrate differences in expression of PDPN and SOST in mineralized groups, key proteins in osteocyte mechanointeractions. The scale bar in b represents 20µm, in c and d, 500 nm, and h-k 40 µm. The traced lines in f and g represent the values for bone tissue. Experiments were performed using three biological replicates. In f and g, the statistical differences are represented by **$p < 0.01$ after a Student's t-test. Parts of this figure were made with Biorender.*

2.2. Paracrine signaling accelerates functional osteoclastogenesis

Osteocytes play a central role in regulating bone homeostasis by coordinating the response of osteoblasts and osteoclasts through key signaling pathways. One of the key mechanisms regulating bone remodeling is the modulation of the ratio between receptor activator of nuclear factor κB ligand (RANKL) and osteoprotegerin (OPG)[46], where RANKL promotes osteoclastogenesis, and OPG serves as its inhibitor (Fig. 2a). Osteocyte signaling, influenced by mechanical factors like matrix stiffness and fluid shear stress, bridges biomechanical and biochemical cues, facilitating the recruitment of monocytes and their differentiation into osteoclasts[47, 48]. While these interactions are well-characterized in-vivo, replicating them in-vitro remains challenging, particularly when sustaining multiple differentiated cell types in culture using exogenous growth factors alone can prove difficult and result in unintended cross-talk. In our system, following matrix mineralization, during which osteoblasts matured into osteocytes, we leveraged the resulting microenvironment to recreate the coordinated triad of bone cell activity spatially. To do so, we introduced additional osteoblasts and human monocyte-derived macrophages into the lateral channel of the microfluidic chip. The added osteoblasts were intended to line the mineralized matrix surface, supporting the differentiation of immune precursor cells into osteoclasts. This configuration simulates the physiological recruitment of monocytes/macrophages from the bone marrow or vasculature to the bone surface, where they undergo osteoclastogenesis in response to sustained osteocyte-derived cues. The osteoclast phenotype in mineralized chips was compared with control samples either left untreated or treated with RANKL (50 ng/mL) and macrophage colony-stimulating factor (M-CSF, 30 ng/mL), representing the traditional growth factor-mediated osteoclast differentiation protocol (named NM + GF).[49]

A multiplex Luminex assay measuring 13 cytokines and proteins revealed significant differences in paracrine signaling profiles among the groups over time. By day 3, the mineralized samples demonstrated elevated levels of pro-osteoclastogenesis mediators such as metalloproteinase 9 (MMP9), RANKL, and macrophage inflammatory protein 1 alpha (MIP-1α) in comparison to both non-mineralized groups, while OPG production was significantly downregulated (Fig. 2b). Given the specific roles of RANKL and OPG in driving and inhibiting osteoclastogenesis, respectively, this shift in the RANKL/OPG balance reflects transition to a pro-osteoclastogenic state (Fig. 2b and Supplementary Fig.6 and Supplementary Fig.7). In mineralized groups, RANKL levels peaked at day 3 but returned to baseline by day 5, suggesting a transient and tightly regulated osteoclastogenic response driven exclusively by embedded osteocytes through crosstalk with osteoclast-precursor macrophages, in the absence of other exogenous media supplements. On the other hand, RANKL and M-CSF-treated controls elicited a pronounced and sustained pro-inflammatory response characterized by increased production of TNF-α and IL-1β (Fig. 2b and Supplementary Fig. 6 and Supplementary Fig. 7). Importantly, our findings align with key mechanobiologically driven events described in-vivo where matrix stiffness modulates RANKL/OPG signaling to drive osteoclastogenesis[50]. Additionally, the upregulation of MIP proteins observed in the mineralized groups further supports the physiological relevance of this model, given that these chemokines are known to be involved in the recruitment of macrophages to the bone surface, which is critical to initiate osteoclastogenesis[51].

Osteoclastogenesis in conventional 2D culture systems typically requires 14–21 days of RANKL/M-CSF stimulation. However, with the bone mechanical and paracrine cues engineered into our system, by days 3 and 5, multinucleated osteoclasts were significantly more abundant in the mineralized groups than in non-mineralized controls with or without RANKL and M-CSF (Fig. 2c, g, k, and o). We also observed that the number of multinucleated cells expressing cathepsin K (Fig. 2d, h, i and p), MMP9 (Fig. 3e, f, m, and q), and TRAP (Fig. 3f, j, n, and r) was significantly higher in the mineralized than non-mineralized groups with or without growth factors. Elevated levels of these proteins are consistent with both enhanced osteoclast formation and their functional capacity to resorb mineralized matrix. Addition of RANKL and M-CSF to mineralized groups (named MIN + GF) significantly increased the number of cathepsin K, TRAP, and MMP9 multinucleated cells, demonstrating the system's tunability for modeling

individualized bone remodeling responses (Supplementary Fig. 8). These results highlight the system's capacity to replicate a mineralized bone environment that supports rapid and efficient osteoclastogenesis, driven by the osteocyte-osteoclast mediated RANKL/OPG axis, and independent of prolonged inflammatory signaling present in growth factor supplemented osteoclastic media.

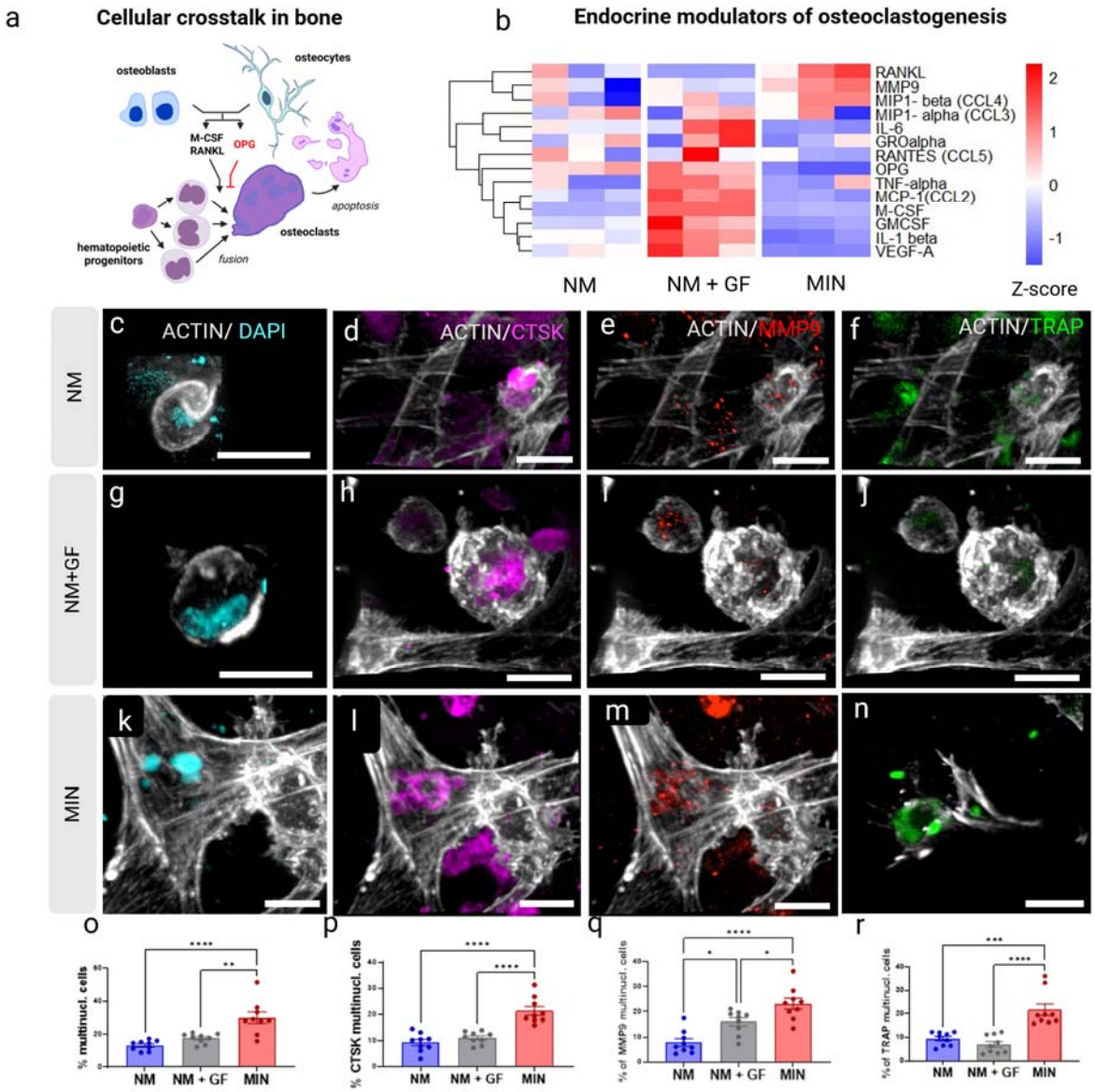

Figure 2 – Paracrine signaling mediated by the bone-like microenvironment triggers rapid osteoclastogenesis. *The bone microenvironment was established by embedding osteoblasts in a collagen matrix and mineralizing it over a period of 3 days. Osteoblasts and macrophages were introduced into the*

*lateral channel to emulate osteoclastogenesis mediated by osteocytes and osteoblasts (a). The supernatant was collected to assess the secretion of osteoclastogenic factors. (b) Heatmap of protein levels measured via Luminex after 3 days of incubation with macrophages and osteoblasts, expressed as Z-scores. The mineralized samples showed elevated RANKL levels and reduced OPG levels compared to non-mineralized samples (NM) and non-mineralized samples treated with RANKL and M-CSF (NM + GF). (c-n) Representative images of samples immunostained for cathepsin-K (magenta), MMP9 (red), TRAP (green), ACTIN and DAPI (blue, nuclei) illustrate the morphological differences (number of nuclei and spread cells) along with osteoclast marker expression and function in non-mineralized, non-mineralized with growth factors, or mineralized matrices after 5 days of incubation. Mineralized samples exhibited characteristic multinucleated osteoclast morphology (o) and higher expression levels of CTSK (p), MMP9 (q), and TRAP (r), compared to the other groups. Scale bars in (c-n) represent 20 µm. Experiments were performed using three biological replicates, with statistical significance represented by **$p < 0.01$, ***$p < 0.001$, and ****$p < 0.0001$ after a one-way ANOVA with Bonferroni corrections.*

2.3. Osteoclastogenesis through ECM-dependent pathways and not inflammatory signaling

To elucidate the molecular mechanisms underpinning the accelerated biomimetic osteoclastogenesis observed in Fig. 3c-h, we performed targeted gene expression profiling to compare differentiating cells exposed to mineralized versus non-mineralized matrices. Osteoclastogenesis is classically regulated by the RANKL/RANK and M-CSF signaling pathways, which converge on activation of NF-κB to initiate transcriptional programs associated with osteoclast differentiation and activity[52]. While these pathways are well-characterized in 2D cultures supplemented with exogenous RANKL and M-CSF, the signaling mechanisms engaged by a mineralized matrix enriched with osteocyte-derived factors remain poorly explored in-vitro[49]. Our platform provides a unique opportunity to dissect these pathways as influenced by paracrine cross-talk.

To evaluate how our engineered mineralized matrix compares to the traditional growth factor-driven method of osteoclastogenesis, we compared the gene expression profiles of osteoclast precursor macrophage cells cultured on biomimetically mineralized matrices with those on standard collagen matrices supplemented with exogenous RANKL/M-CSF. RNA isolated after three days of incubation was analyzed using a NanoString nCounter panel targeting a panel of 825 genes (Supplementary Table 1). Both groups exhibited enrichment of classical

osteoclast markers, such as *ACP5 (TRAP)* and *CTSK* (Supplementary Fig. 11). However, inflammatory genes such as *IL1B*, *STAT1*, and *FSTL1* were significantly elevated in the RANKL/M-CSF treated group, whereas genes related to cellular adhesion, migration, bone resorption, and ion homeostasis were prominently upregulated in the mineralized matrix group (Fig. 3a).

Focusing on a curated set of key osteoclast-related genes (Fig. 3c), we observed marked upregulation of matrix-modifying transcripts in the mineralized matrix group, including CTSK, a key protease involved in bone matrix degradation (Fig. 3i). These data suggest that mineralized environments promote osteoclastogenesis through gene pathways that are mechanistically distinct from the inflammatory signaling typically induced by RANKL/M-CSF treatment. Gene ontology analysis of the top 100 upregulated genes in the mineralized matrix group further revealed significant enrichment in cellular response pathways, cell-matrix adhesion, and cell migration (Fig. 3c). Together, these findings highlight the capacity of mineralized matrices to establish a physiologically relevant microenvironment that supports osteoclast differentiation through adhesion- and matrix-mediated cues independent of exogenous growth factor supplementation. This finding points to exciting possibilities in the field of engineered models that have traditionally relied on supraphysiological supplementation of cells with growth factors to stimulate biological activity, which for the first time we show not to be necessary to drive complex multicellular cross-talk and functional response in an engineered model.

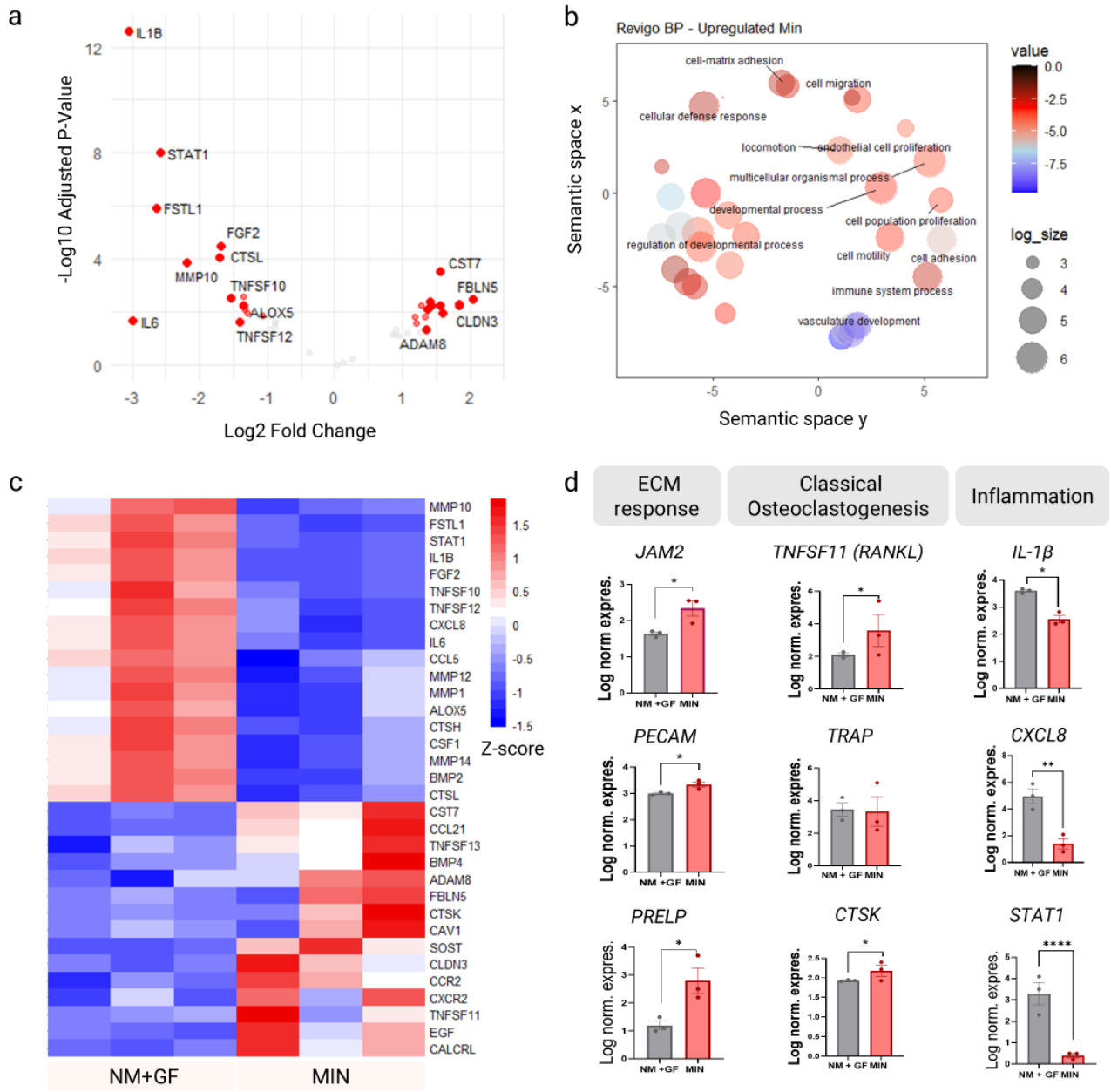

Figure 3. Distinct gene signatures are associated with rapid biomimetic osteoclastogenesis. *Osteoclasts differentiated in mineralized samples (MIN) express canonical osteoclast-related genes distinct from those in non-mineralized matrices treated with RANKL and MCS-F (NM + GF). The volcano plot in (a) represents the significantly differentially expressed genes among the 825-gene NanoString panel, comparing mineralized vs. non-mineralized with growth factors. Points represent* $\log_2$ *fold change and adjusted p-value; red points denote genes with significant differential expression. In (b), a semantic similarity plot was generated with ReviGO, based on GO terms enriched among the top 100 upregulated genes in mineralized conditions (vs. NM + GF). Gene ontology analysis was performed using the Princeton GO Term Finder, and biological process terms with* $p<0.1$ *were labeled. (c) Heatmap showing average expression of significantly altered osteoclast-related genes across all replicates. Gene expression is color-scaled, with red indicating higher and blue lower expression. Each column represents an individual replicate (n = 3 per condition). (d) Log2 fold change of selected genes upregulated in*

*mineralized matrices, grouped by category: extracellular matrix response, classic osteoclast markers, and inflammatory response. Genes were selected from the NanoString panel based on a literature review. Experiments were performed using three biological replicates. Statistical significance was assessed by an unpaired t-test: ** p□0.01, and **** p□0.0001 after a t-test.*

To demonstrate the platform's adaptability for modeling complex, vasculature-driven multicellular interactions, microvascular capillaries were engineered by co-culturing Human Umbilical Vein Endothelial Cells (HUVECs) with human mesenchymal stem cells (hMSCs) and osteoblasts in both mineralized and non-mineralized matrices. Perfusable vascular networks formed within two days, preceding the three-day mineralization phase. Quantitative analysis revealed no significant differences in total vessel length or area between mineralized and non-mineralized conditions, indicating that mineralization did not impair vascular morphogenesis (Supplementary Fig.9). Following vascularization, macrophages were introduced into the lateral channel, and intact $CD31^+$ vessels were observed adjacent to cathepsin-K^+ osteoclasts in both matrix conditions (Supplementary Fig. 9g-h). Importantly, this modular approach enables the stepwise integration of relevant tissue components, such as vasculature, to facilitate investigations of how vascular cues contribute to bone physiology and disease progression.

2.4. Functional osteocyte-osteoclast responses to anti-resorptive therapies

Next, to evaluate whether our platform supports the functional response of osteoclasts from precursor cells, we compared mineral degradation on samples engineered with and without monocyte-derived macrophages. Bone resorption was assessed by quantifying pit areas using second harmonic generation (SHG) imaging and by visualizing mineral degradation with microCT (Fig. 4a and Supplementary Fig. 15). These analyses revealed a marked increase in matrix degradation on chips containing osteoclasts compared to control groups lacking osteoclasts (Fig. 4a-d), confirming robust osteoclastic activity. Notably, this dynamic, quantifiable resorption has not previously been demonstrated using radiologic methods in an on-a-chip setting. We further evaluated the functionality of osteoclasts differentiated in the chip by comparing their bone-resorbing ability to that of conventionally differentiated osteoclasts. Osteoclasts retrieved from the chip were seeded onto calcium phosphate-coated resorption plates and assessed for pit-forming activity over three days. Pit areas were comparable between chip-derived osteoclasts and those differentiated using exogenous RANKL and MCS-F

(Supplementary Fig. 16), further indicating that osteoclasts matured on-a-chip retain functional bone-resorptive capacity even after removal from the device.

The inability of existing in-vitro models to capture key features of the bone microenvironment undermines their predictive power for evaluating anti-resorptive drugs. To establish our bone-on-a-chip system as a high-fidelity platform for preclinical drug testing, we evaluated the effects of two clinically available anti-resorptive agents: alendronate, a bisphosphonate, and denosumab, a monoclonal antibody targeting RANKL. Both drugs are widely utilized in the treatment of osteoporosis and bone metastases, although clinical evidence consistently indicates denosumab's superior efficacy[53]. Replicating these differential outcomes in-vitro has been challenging due to the distinct mechanisms of action of these drugs and their reliance on complex microenvironmental contexts. Denosumab inhibits osteoclastogenesis by binding to RANKL, thereby disrupting signaling along the osteoblast-osteocyte-osteoclast axis[54]. In contrast, alendronate is internalized by osteoclasts after binding to hydroxyapatite and interferes with cytoskeletal organization[55]. Importantly, these mechanisms are modulated by osteocyte-mediated signaling within a mineralized matrix, an element largely absent in conventional in-vitro models. To capture this complexity, macrophages were introduced into the bone-on-a-chip system after a 3-day mineralization period, followed by treatment with either alendronate (10□□ M) or denosumab (30 μg/mL) for 5 days. Samples were fixed and analyzed for cellular morphology, multinucleated cell formation, tartrate-resistant acid phosphatase (TRAP) expression, and functional osteoclast activity. Results were benchmarked against commercial calcium phosphate (CaP)-coated plates, which represent an industry-standard model of osteoclastogenesis using RANKL and MCS-F. Both drugs effectively suppressed osteoclastogenesis, as evidenced by a reduction in TRAP-positive multinucleated cells on both the chip and CaP plates (Fig. 4e-j). However, only on-chip assays assessing matrix resorption revealed a significant divergence in drug efficacy that matches the reported clinical efficacy of these drugs. Accordingly, on-chip experiments showed that denosumab significantly reduced bone resorption with smaller pit areas relative to both untreated controls and alendronate-treated samples. Experiments off-chip did not recapitulate these clinically reported results (Fig. 4l-q), highlighting the sensitivity of the bone-on-a-chip model in comparison to established methods.

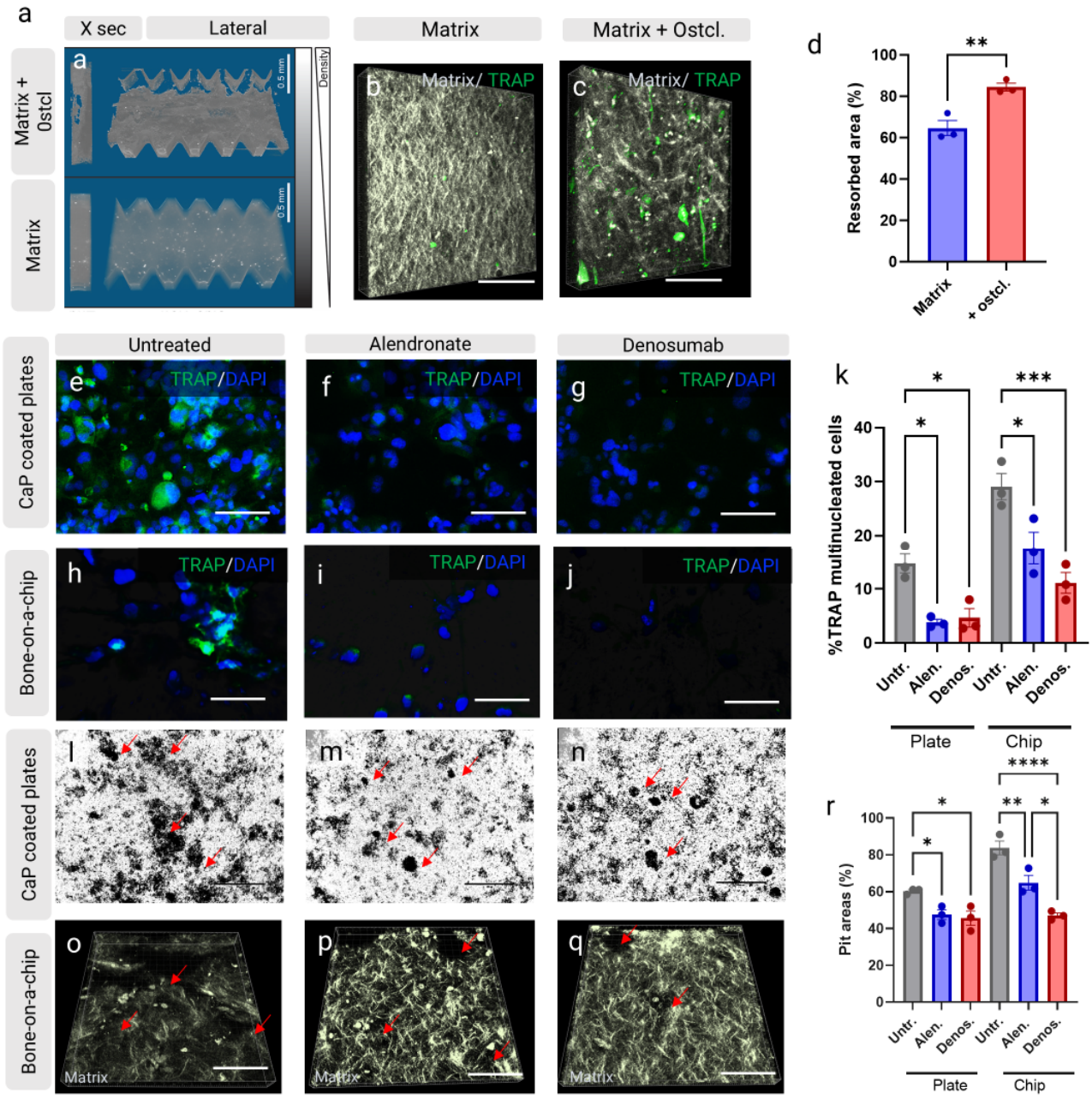

Figure 4. Bone biomimetic environment stimulates functional osteoclast activity and enhances sensitivity to anti-resorptive drugs. *(a) Cross-sectional and lateral views of mineralized matrix with and without osteoclast exposure, visualized via microCT. (b-c) Second harmonic generation (SHG) microscopy of matrix-only (b) and matrix with osteoclasts (c) shows increased resorption-associated disruption. (d) Quantification of resorbed area (%) confirms enhanced matrix degradation with osteoclasts. (e-j) Representative TRAP staining of multinucleated osteoclasts formed in CaP-coated plates (e-g) or the bone-on-a-chip system (h-j), following treatment with vehicle, alendronate (10□□ M), or denosumab (30 µg/mL). (k) Quantification of TRAP^{+} multinucleated cells shows reduced osteoclast formation with both treatments on both platforms. (l-q) Resorption pits visualized in grayscale on CaP-coated plates (l-n) and using SHG on-chip (o-q), with red arrows indicating resorption pits. (r) Quantification of pit areas (%) reveals suppression by both drugs, but only the chip platform*

*distinguished differential effects between alendronate and denosumab. Data represent mean ± SEM from three biological replicates. Statistical comparisons used one-way ANOVA with Bonferroni correction: *p < 0.05, **p < 0.01, ***p < 0.001, ****p < 0.0001. Scale bars: 100 µm (b-c, e-j, o-q), 400 µm (l-n).*

2.5. Recapitulating the invasion of oral cancer cells into bone

To evaluate the ability of the bone-on-a-chip system to model complex, disease-relevant phenomena that depend on cross-communication between heterogeneous bone-resident cell populations, a challenge that remain difficult to address in-vitro, we investigated oral squamous cell carcinoma (OSCC) invasion into bone, a common and devastating process responsible for extensive bone destruction in oral cancer. While osteoclasts are known to facilitate bone invasion via paracrine signaling, existing in-vitro models fail to replicate the spatial and histological complexity observed in-vivo[56]. To address this gap, we compared OSCC invasion dynamics in engineered microenvironments with or without osteoclasts. Following osteoclast differentiation in the bone-on-a-chip system as described above, OSCC cells were seeded into one of the lateral channels of the microfluidic device after 3 days and co-cultured with bone cells (osteoblasts and pre-osteoclasts) for 24h. Invasion was then evaluated in the presence or absence of osteoclasts. Pan-cytokeratin (PAN-CK) staining was used to identify OSCC cells and visualize their spatial distribution relative to the mineralized matrix over time (Fig. 5a). Notably, pan-cytokeratin-positive OSCC cells in the osteoclast-containing group exhibited reduced aspect ratios, suggesting a shift toward a more rounded or invasive phenotype (Fig. 5c, f, and n).

While small, localized disruptions of the tumor-matrix interface were evident even in the absence of osteoclasts (Fig. 5c-d), more extensive disruption of the interface was observed in the groups containing osteoclasts, consistent with enhanced invasive potential (Fig. 5f-g). These findings were corroborated by collagen SHG imaging, which revealed significant degradation of the mineralized matrix in osteoclast-containing conditions (Fig. 5d, g). Quantitatively, a higher number of PAN-CK^{+} cells (OSCC) infiltrated the matrix in the presence of osteoclasts (Fig. 5o). Histological analysis using hematoxylin and eosin staining further confirmed the presence of OSCC invasion pockets, which were more prominent and consistent in osteoclast-containing groups (Fig. 5j-o). These results demonstrate that our bone-on-a-chip system faithfully replicates critical aspects of the OSCC-bone interface, offering a robust platform to dissect previously

inaccessible questions in OSCC pathobiology, such as the earliest initiation events of bone invasion.

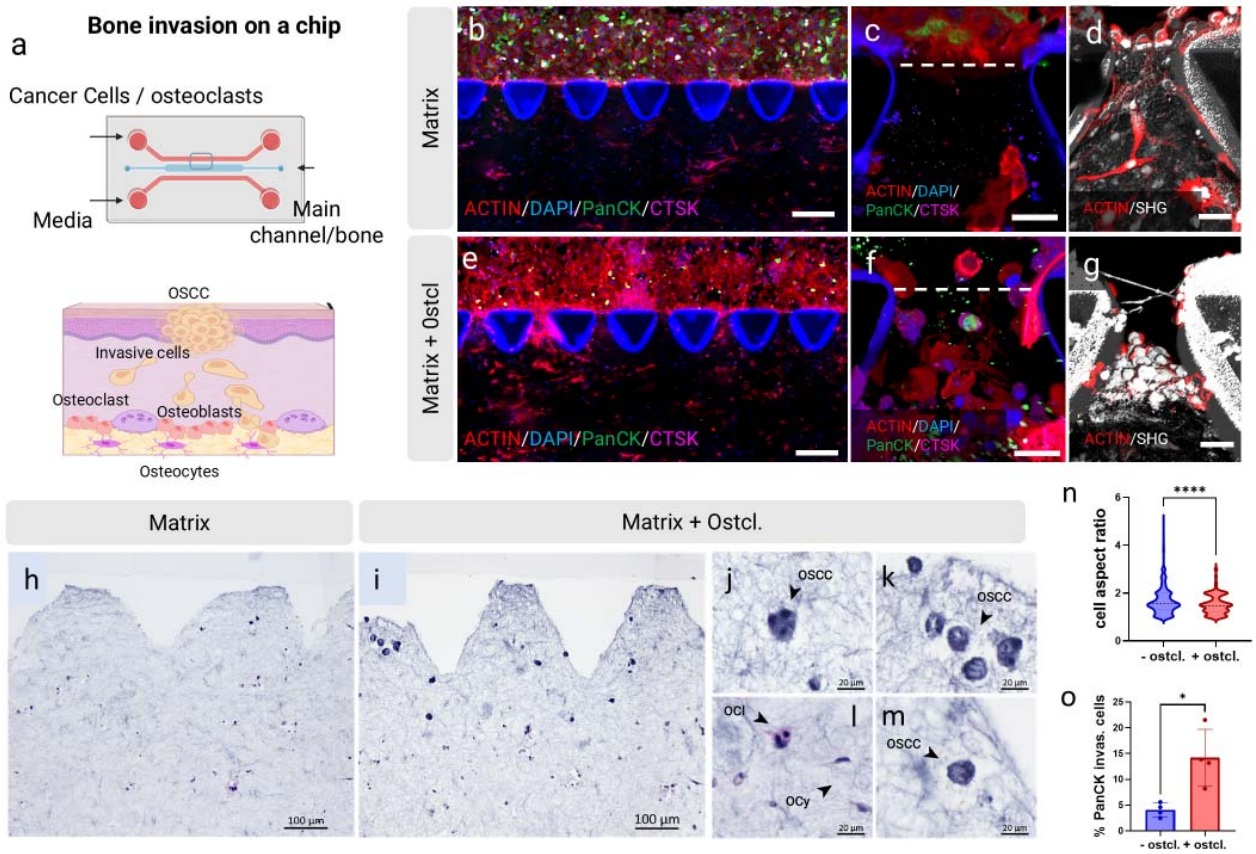

Figure 5. Bone-on-a-chip replicates key cellular and spatial features of OSCC bone invasion. *(a) OSCC cells were introduced into lateral channels after bone channel formation, and invasion was assessed in the presence or absence of osteoclasts. Representative images show OSCC cells (PAN-CK^{+}, green) invading into mineralized matrix (b-g). OSCC invasion was more pronounced in osteoclast-containing samples, as evidenced by deeper penetration and the formation of bone resorption pockets (arrows in j), also visible in second harmonic generation (SHG) imaging (d, g). H&E-stained sections (h-m) confirm these findings, revealing cancer cells (OSCC), osteoclasts (OCl), and osteocytes (OCy) within the matrix. Quantification shows significantly lower ratios in OSCC cells exposed to osteoclasts (n), and a higher percentage of invading OSCC cells in the absence of osteoclasts (o), suggesting differential invasion dynamics. Scale bars: 250 µm (b-c), 50 µm (c,d,f,g). Statistical differences are represented by *p < 0.05, ****p < 0.0001 after a T-test. Parts of this figure were made with Biorender.*

3. Discussion

Recent advances in bone tissue engineering, particularly in bone-on-a-chip platforms, have significantly improved our ability to model aspects of bone biology in-vitro[35, 57]. However,

recreating a self-regulated system that supports rapid osteocyte differentiation, osteoclastogenesis, and vascularization within a 3D homogeneously calcified microenvironment, and without exogenous growth factors, remains a fundamental obstacle[58]. To address this limitation, we demonstrate that engineering essential biomechanical and biochemical cues, specifically intrafibrillar mineralization and embedded osteocyte networks, drives spontaneous and rapid osteoclastogenesis that mirrors hallmark features of bone remodeling. Moreover, the platform can be engineered to incorporate additional bone components, such as embedded vascular capillaries supported by stem cell-derived pericytes, enabling selective addition or removal of key cellular and matrix features that define bone function. Remarkably, in the absence of exogenous osteogenic factors, osteoblasts embedded within a mineralized matrix matured within three days, forming interconnected cellular networks and upregulating canonical osteocyte markers, including PDPN. As shown in Fig. 1, this biomimetic osteocytic differentiation represents a key milestone in reproducing the physiological dynamics of bone remodeling and exceeds the capabilities of existing 3D or on-chip bone models. PDPN, a transmembrane glycoprotein, is typically induced when osteoblasts are subjected to mechanical stimuli within a mineralized environment and plays a crucial role in establishing the osteocytic network by mediating dendritic connectivity[59]. Collectively, these findings establish that our engineered system recapitulates the osteoblast-to-osteocyte transition in-vitro, capturing essential features of bone physiology and remodeling.

Our study establishes a self-regulating microenvironment that supports autonomous osteoclastogenesis[60]. The observed upregulation of RANKL and MMP9, alongside suppression of OPG, reflects intrinsic paracrine signaling between bone-forming and bone-resorbing cells, modulating osteoclast differentiation and activity. This signaling cascade, initiated by matrix mineralization and the presence of embedded osteocytes, supports rapid formation of multinucleated osteoclasts and functional bone resorption, as validated by pit formation assays. Notably, macrophages differentiated into osteoclasts in the absence of exogenous growth factors and localized specifically to the mineralized matrix zones, suggesting effective niche recognition and activation. Cell fusion events were observed within hours, highlighting the efficiency and fidelity of this model in recapitulating physiological osteoclastogenesis. These findings are consistent with prior reports linking increased matrix stiffness to enhanced osteoclastogenesis, evidenced by the upregulation of canonical markers such as CTSK**,** MMP9, and ACP5[48, 61].

However, in contrast to conventional systems that rely on supraphysiological levels of RANKL and M-CSF, our biomimetic platform leverages osteocyte-derived cues to induce osteoclastogenesis. This physiologically relevant approach uncovered adhesion and junction-associated genes as potential regulators of osteoclast differentiation, features previously underappreciated[62]. Notably, genes such as *FBLN5***,** *CLDN3*, and *ADAM8* were significantly upregulated in the mineralized condition, suggesting a matrix-dependent transcriptional program. *FBLN5* was particularly noteworthy for its dual role in promoting *RANKL* expression while suppressing osteogenic signaling, potentially acting as a molecular switch favoring osteoclatogenesis[63]. *CLDN3*, a tight junction protein, may influence osteoclast-matrix interactions by modulating cell adhesion dynamics[64]. Elevated *ADAM8* expression, a known mediator of osteoclast precursor fusion, further supports its essential role in matrix-guided osteoclastogenesis; inhibition of *ADAM8* has been shown to markedly impair osteoclast formation[65]. By contrast, samples treated with RANKL/M-CSF exhibited a transcriptional profile dominated by inflammatory mediators, including pronounced elevation of *IL1B*, in alignment with Luminex cytokine profiling (Figure 2b and Supplementary Figure S7). This divergence highlights two possible distinct regulatory gene-associated pathways for osteoclast differentiation - one driven by inflammatory cues under exogenous stimulation, and another by matrix-embedded biophysical and paracrine signals orchestrated by osteocytes in a mineralized environment. It is important to emphasize that this observation is based on a single-gene snapshot, highlighting the necessity of further validation across wider regulatory pathways.

The translational utility of our platform is illustrated by its ability to model therapeutic responses with high fidelity, capturing clinically observed outcomes in-vitro. Clinical trials have consistently shown that denosumab outperforms other antiresorptives in increasing bone mineral density and reducing fracture risk [53], yet recapitulating these effects in-vitro has proven difficult. Our system not only reflects these therapeutic trends but also establishes a robust preclinical framework for evaluating bone-targeted drugs. Importantly, most in-vitro models lack both osteocytes and the complete osteoblast-osteoclast-osteocyte axis, often also excluding vascular or mechanical cues that modulate drug response. This omission limits mechanistic insight, particularly as osteocytes regulate bone remodeling through the RANKL/OPG signaling axis[66]. For example, the effects of alendronate on osteocyte biology remain poorly defined, despite its widespread clinical use[67]. Similarly, denosumab's suppression of RANKL activity elevates OPG

and halts resorption[68]; however, this sustained suppression may underlie the rebound bone loss observed after treatment discontinuation[69], a phenomenon that cannot be investigated in osteocyte-deficient models. By enabling integrated readouts across cell types within a physiologically mineralized biomimetic matrix, our platform provides a uniquely sensitive system for dissecting drug mechanisms, dose-response dynamics, and treatment withdrawal effects. Moreover, its modular design permits the incorporation of patient-derived cells, laying the groundwork for personalized medicine approaches in bone disease therapy.

Beyond its capacity to model resorption, our platform offers a unique opportunity to interrogate broader roles of osteoclasts in bone regeneration, osteocyte-mediated signaling, and cancer-bone interactions, including tumor invasion and metastasis[70, 71, 72]. One clinically significant application demonstrated here is the modeling of oral squamous cell carcinoma (OSCC) invasion, a process that targets mineralized tissues and contributes to catastrophic bone loss in oral cancer. Despite being the sixth most prevalent cancer worldwide[73, 74], oral malignancies remain underrepresented in the development of advanced in-vitro models. Our system successfully recapitulates osteolytic behaviors characteristic of OSCC bone invasion, capturing for the first time in-vitro the spatial and cellular features observed in patient samples. This capability enables dynamic monitoring of tumor-bone interactions, which have historically been limited to static, end-point observations in-vivo. While prior studies have described bone invasion across multiple cancer types[56, 75, 76], fundamental questions remain regarding the mechanisms driving OSCC tropism toward bone. Notably, we observed that OSCC cells attempted to penetrate the mineralized matrix even in the absence of osteoclasts, implicating the role of matrix composition, mechanical stiffness, and paracrine signals in mediating invasion[77]. Additionally, OSCC cells exhibited morphological transitions at the tumor-bone interface, suggestive of a potential epithelial-to-mesenchymal transition (EMT), triggered by biophysical and biochemical cues from the mineralized matrix[78, 79]. Such mechanotransduction events have been shown to activate EMT and enhance invasive potential[80], highlighting the relevance of our system for dissecting the early steps of cancer cell adaptation to the bone microenvironment.

Despite these advances, certain limitations remain. The current model does not yet incorporate components of the adaptive immune system, such as T and B lymphocytes, which are known to influence both bone remodeling and tumor progression[81]. Additionally, while

vascular and neural elements have previously been integrated into our mineralized matrix platform[38], further optimization is needed to address specific biological questions before these features can be systematically included in disease contexts. Incorporating these components will expand the model's utility for studying immune-mediated bone disorders and further enrich the complexity of the tumor microenvironment. Looking ahead, the vascularized architecture of our model offers a promising foundation for investigating perfusion dynamics, immune cell trafficking, and mechanisms of metastatic dissemination within a controlled, bone-like microenvironment. With its modular, plug-and-play design, this versatile platform is well-suited for studying bone biology across both physiological and pathological states, spanning development, homeostasis, and disease.

In summary, our biomimetic bone-on-a-chip model constitutes a significant advance in tissue-engineered New Approach Methodology platforms for bone research. By recapitulating the structural, cellular, and biochemical intricacies of native bone, this system offers an unprecedented opportunity to investigate bone physiology, model disease progression, and evaluate therapeutic responses under physiologically relevant conditions. Its modular architecture and biological responsiveness position it as a versatile tool for both fundamental research and translational applications. As such, this innovation holds strong potential to accelerate the development of precision therapies and deepen our understanding of skeletal pathophysiology across diverse clinical contexts. More broadly, it marks a critical step toward the realization of high-complexity in-vitro human models capable of complementing – or even replacing - animal models in the pursuit of mechanistic insights and human-relevant therapeutic discovery.

4. Methods

Cell Culture

Human osteoblasts hFOB 1.19 (ATCC, CRL-3602) were cultivated in human osteoblast media (Cell applications) supplemented with 10% fetal bovine serum (FBS) (Thermo Fisher) and 1% Penicillin/Streptomycin (P/S) (Thermo Fisher). The cells were used in passages 6-12. Human THP-1 monocyte cell lines (ATCC) were cultivated in Roswell Park Memorial Institute (RPMI

1640 media, Thermo Fisher) supplemented with 10% FBS, 1% P/S. Passages 10-15 were used to ensure consistent differentiation capacity. THP-1 cells were differentiated into macrophages by adding a solution of Phorbol 12-myristate 13-acetate (PMA, Sigma-Aldrich) (100 ng/mL) for 48h. Cells were maintained at 37 ^{o}C in a humidified incubator with 5% CO_2. OSCC cells UCSF-OT-1109 (ATCC) were cultured in RPMI media supplemented with 10% FBS and 1% P/S. Osteoblasts were transduced with *pEF1α-tdTomato* lentiviral particles (Takara Bio) at a multiplicity of infection (MOI) of 5. Following transduction, cells were selected with puromycin (1 µg/mL) to establish a stable tdTomato-expressing population.

Microfluidic device and osteoblast-laden gel

To establish the biomimetic tissue on a chip, we used a DAX-1 microfluidic device (AIM Biotech). Each device contains a main channel (1.30 mm wide x 0.25 mm high) flanked by two secondary media channels (0.5 mm wide x 0.25 mm high). Prior to gel loading, chips were coated with 1 mg/mL of poly-D-lysine (PDL; Merck) for three hours at 37°C to improve collagen adherence. To prepare the osteoblast-laden hydrogel, acid-solubilized type I collagen from rat tail (3 mg/mL, Thermo Fisher) was diluted to a final concentration of 2.5 mg/mL in 10x phosphate-buffered saline (PBS) with α-MEM media (Gibco, Thermo Fisher), neutralized with 1 N sodium hydroxide (NaOH) to pH 7.4. The mixture was combined with a suspension of osteoblasts for a final concentration of 3 × 10□ cells/mL. A 10 µL volume of the resulting pre-gel solution was pipetted into the central channel of each microfluidic device. The samples were maintained in a humidified incubator at 37 °C for 45 min to allow self-assembly fibrillogenesis.

Nanoscale mineralization

To induce the collagen mineralization, a mineralizing medium was prepared containing 9□mM $CaCl_2$·2H2O (J.T. Baker) and 4.2□mM K_2HPO_4 (J.T. Baker) in α-MEM supplemented with 10% FBS and 1% P/S, based on our previously described protocol (REF). Lacprodan® OPN-10 (Arla Foods Ingredients Group P/S), a bovine milk-derived osteopontin analogue, was added to the $CaCl_2$-containing solution at a concentration of 100□µg/mL before the addition of K_2HPO_4. To maintain a stable pH of 7.4, 25□mM HEPES was added to the mineralizing medium. The media was added to the side reservoirs of the microfluidic chips and the devices were placed on a 2D rocker platform inside a humidified incubator (37 °C, 5% CO_2, 95% humidity) to allow continuous flow and homogeneous mineralization throughout the gel. The media was replaced

daily for 3 consecutive days to allow full mineralization of the biomimetic bone-on-a-chip construct.

Matrix characterization

SEM - Mineralized and non-mineralized samples were fixed with 2% glutaraldehyde on a 2D rocker at room temperature for 2 hours, followed by washing with distilled water. Samples were dehydrated in an ascending ethanol series, removed from the chip, and subjected to critical point drying. The dried samples were mounted, sputter-coated with a 10 nm platinum coating, and imaged using a Helios Nanolab™ G3 DualBeam™ SEM (FEI, Thermo Fisher) (N□=□3).

FTIR - Fourier Transform Infrared (FTIR) spectroscopy was performed using a Nicolet 6700 spectrometer (Thermo Scientific) in transmission mode. Spectra were recorded with 32 scans across a range of 4000–400 cm□¹, with a resolution of 4 cm□¹. The mineral-to-matrix ratio was determined by comparing the area of the ν□PO□ peak (1030 cm□¹) to that of the amide I peak (1660 cm□¹) after applying baseline correction and normalization to the amount of amide present. The crystallinity index was assessed using the splitting factor, calculated from the doublet peaks in the fingerprint region (500–650 cm□¹), primarily attributed to □□PO□³□ bending vibrations. This calculation involved summing the peak heights at 565 cm□¹ and 605 cm□¹ and dividing by the height of the trough between them at 590 cm□¹. Peak height measurements were conducted using Spectragryph software, with spectra normalized to the intensity of the amide I band (1585–1720 cm□¹) following baseline correction (N=3).

Alizarin red - An alizarin red assay was performed further to confirm the presence of calcium deposition inside the hydrogel. The samples were stained with a 2% (w/v) alizarin red S solution, incubated for 15 minutes, and then washed in water until the solution was clear. The stained areas were analyzed by inverted microscopy (FL Autos, EVOS – Thermo Fisher Scientific) (N=3).

Osteocyte characterization

Cellular viability – After 3 days of mineralization, the cells inside the matrix were stained with a Live/Dead Cell Imaging Kit (Molecular Probes, Thermo Fisher) to confirm their viability. Following incubation, the specimens were washed with PBS and imaged using an inverted fluorescence microscope (n = 3) (FL Autos, EVOS – Thermo Fisher Scientific, Waltham, MA,

USA). Image processing and analysis were performed using ImageJ (FIJI) software[82] to assess cell viability, calculated as the ratio of total nuclei (blue, stained with 4′,6-diamidino-2-phenylindole, DAPI) to dead cells (red, stained with Propidium Iodide).

Comparison of mineralized matrix and osteogenic induction: To compare the effects of the mineralized matrix with conventional osteogenic induction, collagen-containing osteoblasts (3 × 10 cells/mL) were either cultured for 3 days to allow matrix mineralization or treated with osteogenic medium (100 nM dexamethasone, 50 μM ascorbic acid, and 10 mM β-glycerol phosphate) for 7 days. PDPN expression was used as an immunofluorescent marker to assess differences between conditions.

Cell morphology and protein expression via immunostaining - Samples (N = 3) were fixed in 10% neutral-buffered formalin for 30 min at room temperature and washed three times with PBS. All subsequent processing (including demineralization, permeabilization, blocking, antibody incubations, and washes) was performed in a microwave-assisted system using the PELCO Biowave Pro+ Tissue Processing System (Ted Pella, Redding, CA). Samples were placed on the PELCO ColdSpot® temperature-controlled surface within the PELCO EM Pro microwave vacuum chamber, sealed against the ColdSpot, and processed under a microwave power of 250 W with a vacuum of approximately 20 mm Hg. The ColdSpot® surface was maintained at 10 °C during demineralization, antibody infiltration, and wash steps, and at 21 °C during permeabilization and blocking. Demineralization was performed in 10% (w/v) EDTA in PBS (pH 7.4). Primary antibodies were then applied under microwave-assisted diffusion. The mouse monoclonal anti-PDPN (Origene DM3500P, 1:200 dilution) primary antibody was used. After washing, the secondary antibody (Alpaca anti-mouse Alexa fluor 488 antibodies, Jackson Laboratories, 615- 545- 214, 1:250 dilution) was applied using microwave-assisted diffusion. F-actin was stained with 555-conjugated phalloidin (molecular probes, Thermo Fisher), and nuclei were counterstained with DAPI (Thermo Fisher). Imaging was performed on a Zeiss LSM 880 confocal microscope, and quantitative analyses of cell morphology and protein expression were carried out with Imaris (v10.1, Oxford Instruments) and FIJI.

Paracrine Signaling via Luminex

Secreted cytokines and growth factors were quantified using a ProcartaPlex multiplex immunoassay (Thermo Fisher), following the manufacturer’s instructions. Supernatants were

collected from biomimetic bone-on-a-chip constructs after 1, 3, and 5 days of incubation under the following conditions: (i) mineralized chips, (ii) mineralized chips treated with RANKL (50 ng/mL, Peprotech) and MCS-F (30 ng/mL, Peprotech), and (iii) non-mineralized controls. The Luminex assay targeted 14 analytes associated with osteoclastogenesis: MCP-1 (CCL2), OPG, VEGF, IL-1β, GM-CSF, TNF-α, MIP-1β (CCL4), RANTES (CCL5), RANKL, M-CSF, MMP-9, GRO-α, MIP-1α (CCL3), and IL-6. Samples were run on a Luminex 200 instrument (Thermo Fisher). The analyte concentrations were determined by extrapolating individual experimental fluorescence intensity values against each analyte's standard curve. The experiment was performed in three biological replicates, and the results were reported as individual concentrations (pg/mL) and as Z-scores for comparative heatmap visualization. For the groups treated with RANKL and M-CSF, the analysis was adjusted by subtracting the baseline concentrations already present in the medium.

Osteoclast characterization

THP-1 cells –THP-1-derived macrophages were seeded onto chips and cultured for 5 days under three conditions: (i) non-mineralized controls, (ii) non-mineralized chips supplemented with RANKL (50 ng/mL) and M-CSF (30 ng/mL), and (iii) mineralized chips. After culture, samples (N = 3) were washed with 1× PBS and fixed in 10% neutral-buffered formalin for 30 min at room temperature. All subsequent steps, including decalcification with EDTA, permeabilization, antibody incubations, and washes, were performed using a microwave-assisted system (PELCO Biowave Pro+, Ted Pella, Redding, CA). Samples were placed on the PELCO ColdSpot® temperature-controlled surface within the PELCO EM Pro microwave vacuum chamber, sealed against the ColdSpot, and processed under a microwave power of 250 W with a vacuum of approximately 20 mm Hg. The ColdSpot® temperature was maintained at 10 °C for antibody infiltration and washing steps, and at 21 °C during permeabilization. Permeabilization was performed with 0.1% Triton X-100, followed by three washes with PBS. Primary antibodies were applied under microwave-assisted diffusion. The following primary antibodies were used: anti-TRAP (Novus Biologicals, NBP2-45294, 1:100), anti-MMP9 (Bioss, bs-4593R, 1:100), and anti-cathepsin K (Thermo Fisher, PA5-18950, 1:100). After washing, secondary antibodies were applied using microwave-assisted diffusion: Donkey anti-goat Alexa Fluor 647 (705-607-003,

1:250 dilution), Donkey anti-mouse Alexa Fluor 790 (SA-000100, 1:250 dilution), and Alpaca anti-mouse Alexa Fluor 488 (615-545-214, 1:500 dilution).

Cell morphology was visualized with Alexa Fluor 555-conjugated phalloidin, and nuclei were counterstained with DAPI (Molecular Probes, Thermo Fisher). Samples were imaged on a CrestOptics X-Light V3 spinning disk confocal system (Nikon Ti2) and a Zeiss LSM 880 laser-scanning confocal microscope (Fast Airyscan). Image analysis was performed with Imaris (v10.1, Oxford Instruments) and FIJI (ImageJ) to quantify multinucleated cells (≥2 nuclei per DAPI staining) and expression levels of TRAP, cathepsin K, and MMP9.

Vasculature formation and vessel quantification

Green fluorescent protein-expressing human umbilical vein endothelial cells (GFP-HUVECs Lonza) were cultured in endothelial cell growth medium supplemented with the EGM-2 bullet kit (Lonza) and base medium from Lifeline Cell Technology (CA). Human mesenchymal stem cells (hMSCs; RoosterBio) were maintained in α-minimum essential medium (Gibco, Carlsbad, CA) supplemented with 10% FBS and 1% P/S. Experiments utilized HUVECs between passages 4 and 6, and hMSCs between passages 2 and 4. All cell cultures were maintained at 37°C in a humidified incubator with 5% CO_2. A suspension containing hMSCS, HUVECs, and osteoblasts in a 4:1:1 ratio (final concentration of 18 mi cells/mL) was dispensed into the main channel of the chip (10 μL total volume). The cell mixture was embedded in a hydrogel composed of 2.5% collagen type I, 2U/mL thrombin, and 1.25 mg/mL fibrinogen. The vessels were allowed to form for 2 days, followed by 3 days of mineralization. THP-1-derived macrophages were added to the lateral channel and co-cultured for 3 days. Samples were fixed and stained for CD31 (Abcam, AB215911, 1:200) and cathepsin K (Invitrogen, PAS18950, 1:100). The vessels were quantified using Imaris (v10.1, Oxford Instruments).

Gene expression and quantification analysis

Samples were collected from three conditions: either non-mineralized, non-mineralized and treated with RANKL and M-CSF, or mineralized. The lateral channels of each chip were washed with PBS and treated with TRI reagent (Zymo Research) for RNA/DNA/protein isolation. Total RNA was extracted and purified using the Direct-zol RNA MicroPrep kit (Zymo Research) following the manufacturer's protocol. RNA concentration and purity were assessed using a

Nanodrop One spectrophotometer (Thermo Fisher). Only samples yielding at least 150 ng of RNA were utilized for downstream analysis. A 1.5 µl aliquot of RNA lysate was used in the nanoString hybridization reaction, and the remainder was stored at −80 °C. nCounter Elements (nanoString) hybridization was performed according to the manufacturer's instructions. The Pan-Cancer Progression panel was used, with the addition of a custom list of 55 bone-specific genes (see Dataset 1 for full gene list). Differential gene expression analysis was performed using the R package DESeq2 (v 1.24.0). Raw count data were normalized using DESeq2's median of ratios method, and differential expression was assessed using the negative binomial generalized linear model (GLM). Genes with an adjusted p-value < 0.01 and absolute fold change ≥ 2 were considered significantly differentially expressed. Two differential gene lists were obtained by adjusting the p-value. Visualization was performed using the heatmap (v1.0.12) R package, displaying the top 50 general genes and a curated list of 33 osteoclast-specific genes. A volcano plot was generated using glMDPlot and glXYPlot from the Glimma package (v1.10.1) to highlight differential expression between non-mineralized + RANKL/M-CSF and mineralized conditions.

Bone remodeling in-vitro

Calcium phosphate resorption assay - Macrophages (THP-1 derived) were seeded at $1x10^5$ cells per well in a 48-well calcium phosphate (CaP)-coated plate (Bone resorption assay plate, AMSBIO) with RPMI media supplemented with10% FBS and 1% P/S. The control groups for the experiment were: untreated macrophages (negative control) and a group treated with RANKL (50 ng/mL) and MCS-F (30 ng/mL) (positive control). After 12 days, we added osteoclasts differentiated on the biomimetic bone-on-a-chip and cultured them further for 2 days. The plates were then washed with PBS and deionized water, followed by 5 min of sodium hypochlorite, according to the manufacturer's instructions. Subsequently, the samples were washed with DI water again and dried out before being taken to a microscope (Evos FL auto 2, Thermo Fisher). Pit areas were analyzed by ImageJ (images transformed into 8-bit and a threshold of 120 units) from 3 different biological replicates.

Second harmonic generation microscopy - Mineralized chip sample matrix structure was compared in the presence or absence (control) of differentiated osteoclasts using second harmonic generation microscopy (SHG). The samples were fixed and immunostained for TRAP

as previously described. The samples (N=3) were imaged using a laser-scanning confocal microscope (Zeiss LSM 880) configured to capture the reflected light between 485 nm and 495 nm, after exciting with a 900 nm laser. The 3D reconstruction was performed using Imaris 10.1 (maximum intensity projection, ch1 channel min-164 and max 6251.69, gamma 1.00), and the analysis of resorbed areas was performed by calculating the black (degraded tissue) to white (preserved tissue) ratio areas in FIJI (images transformed into 8-bit and a threshold of 30 units).

Mineral visualization by X-ray tomography - For assessment of mineralized regions of the bone-on-a-chip, the whole chip assemblies (n=3) were scanned via high-resolution X-ray tomography at 2.3 μm resolution (Zeiss XRadia 620 Versa X-ray Microscope). Chips were scanned after paraformaldehyde fixation (4%), rinsed in PBS, and sealed with Kapton tape. For visualization of the high-resolution X-ray tomography scans, samples were placed at distances from the X-ray source to produce the same energy intensity and resolution at the volume of interest. Scan settings were held constant across all samples as follows: 70 kV voltage, 8.5 W power, 4X objective, 2X binning, and 1-second exposure time. Images were transferred to Dragonfly Pro (Object Research Systems) for visualization. Intensity values varied between scans due to differing amounts of chip material remaining. For qualitative comparison, scans were window-leveled by adjusting the minimum intensity threshold to exclude the plastic chip from view while preserving all higher intensity values.

Anti-resorption drug testing - The most common anti-resorptive drugs, bisphosphonate alendronate sodium (USP Reference standard, Sigma Aldrich, 10^{7} M) and the monoclonal anti-RANKL biosimilar Denosumab (Research Grade, Ichorbio, 30 µg/mL) were chosen for our study. Alendronate sodium was diluted in deionized water, and denosumab was diluted in PBS. The drugs were added to the lateral channel following mineralization and prior to macrophage seeding. The concentration used for alendronate was 10^{-7} M and for denosumab was 30 µg/mL. The media was changed daily for 5 consecutive days, after which cellular viability was evaluated for both drug conditions. The anti-osteoclastogenic effect of the drugs was determined by counting the number of $TRAP^{+}$ and multinucleated cells in comparison with the untreated mineralized group. Osteoclast inhibition by both drugs was determined by quantifying the extent of resorption in FIJI (ImageJ), defined as the ratio of degraded (black pixels) to preserved (white pixels) tissue areas. The drugs were also tested on Ca-P coated plates (in-vitro gold standard for

osteoclast activity) at the same concentrations to compare their osteoclast inhibitory effects for comparison with our biomimetic model.

OSCC bone invasion

OSCC model - For the OSCC bone invasion test, UCSF-OT-1109 cells were cultured in RPMI supplemented with 10% FBS and 1% P/S in passages 5-12. Cancer cells (a total of $3x10^4$ cells) were added into the lateral channel of the microfluidic chips that contained early osteoclasts (after 3 days of osteoclast differentiation). The co-cultures were maintained for 24h to allow paracrine and direct interactions between OSCC cells and bone cells. Samples were fixed and immunostained for markers for osteoclasts (cathepsin-k, Invitrogen PAS18950 1:100) and cancer cells (pan-cytokeratin, Origene SKU TA190320, 1:1000) as previously described.

Histological staining - Tissue was fixed with 4% PFA for 45 minutes, then extracted from the microfluidic device with 2% agarose. Samples were processed for standard formalin-fixed paraffin-embedding by dehydration through a series of graded ethanols, xylene, and infiltration with paraffin wax. Processed tissue was embedded in paraffin wax for microtomy and sectioned at 5 µm thickness. Sections were dewaxed and rehydrated for Hematoxylin and Eosin staining by incubation in hematoxylin, bluing reagent, clearing agent, and eosin before dehydration and coverslipping. Brightfield images were acquired on a Zeiss Axiocam 712 color camera attached with a 0.63x camera mount to a Zeiss Axio Observer 7 inverted microscope stand.

Statistical analysis

All experiments were performed in triplicate unless otherwise specified. For the experiments involving the comparison of two groups, statistical analysis was performed using a two-tailed, unpaired Student's t-test (Prism 10 GraphPad software). For the experiments involving more than two groups, one-way analysis of variance with Turkey's post-hoc test for multiple comparisons was used. The statistical analysis of heatmaps for multiplex analysis by Luminex and gene comparisons (NanoString) was performed using R Studio (version 2023.12.0). A p-value of 0.01 or lower for gene analysis and 0.05 or lower for all the other analyses was considered statistically significant.

Acknowledgements

We acknowledge funding from the Cancer Early Detection Advanced Research (CEDAR) Center at Oregon Health & Science University (OHSU) Knight Cancer Institute. NIH/NCI/NIDCR funding: R01DE029553, R21CA263860, K99DE033689, and T90DE030859, R90DE031533, as well as the Friends of Doernbecher Grant Program at OHSU. We also acknowledge Lacprodan® OPN-10; Arla Foods Ingredients Group for the donation of OPN. Lastly, we acknowledge the Light Microscopy Core at OHSU for support with the image analysis.

Conflict of Interest

Bertassoni LE holds equity and patents associated with HuMarrow Inc., RegendoDent Inc., two companies specializing in advanced tissue engineering, and other IP associated with regeneration technologies. The other authors declared that there are no conflicts of interest.

References

1. Buttgereit, F., Palmowski, A., Bond, M., Adami, G. & Dejaco, C. Osteoporosis and fracture risk are multifactorial in patients with inflammatory rheumatic diseases. *Nat Rev Rheumatol* **20**, 417-431 (2024).

2. Fuggle, N.R. *et al.* Evidence-Based Guideline for the management of osteoporosis in men. *Nat Rev Rheumatol* **20**, 241-251 (2024).

3. Foessl, I., Dimai, H.P. & Obermayer-Pietsch, B. Long-term and sequential treatment for osteoporosis. *Nat Rev Endocrinol* **19**, 520-533 (2023).

4. Organization, W.H. Musculoskeletal conditions. https://www.who.int/news-room/fact-sheets/detail/musculoskeletal-conditions#:~:text=Other%20contributors%20to%20the%20overall,YLDs)%2C%20rheumatoid%20arthritis%20(18; 2022.

5. Fois, M.G., van Griensven, M., Giselbrecht, S., Habibovic, P., Truckenmuller, R.K. & Tahmasebi Birgani, Z.N. Mini-bones: miniaturized bone in vitro models. *Trends Biotechnol* **42**, 910-928 (2024).

6. Qin, L. *et al.* Prospects and challenges for the application of tissue engineering technologies in the treatment of bone infections. *Bone Res* **12**, 28 (2024).

7. Han, Y., You, X., Xing, W., Zhang, Z. & Zou, W. Paracrine and endocrine actions of bone-the functions of secretory proteins from osteoblasts, osteocytes, and osteoclasts. *Bone Res* **6**, 16 (2018).

8. Lutolf, M.P. *et al.* Repair of bone defects using synthetic mimetics of collagenous extracellular matrices. *Nat Biotechnol* **21**, 513-518 (2003).

9. Zhu, S., Chen, W., Masson, A. & Li, Y.P. Cell signaling and transcriptional regulation of osteoblast lineage commitment, differentiation, bone formation, and homeostasis. *Cell Discov* **10**, 71 (2024).

10. Bai, L., Zhou, D., Li, G., Liu, J., Chen, X. & Su, J. Engineering bone/cartilage organoids: strategy, progress, and application. *Bone Res* **12**, 66 (2024).

11. Song, Q. *et al.* Contribution of biomimetic collagen-ligand interaction to intrafibrillar mineralization. *Sci Adv* **5**, eaav9075 (2019).

12. Lewis, K.J. *et al.* Osteocyte calcium signals encode strain magnitude and loading frequency in vivo. *Proc Natl Acad Sci U S A* **114**, 11775-11780 (2017).

13. Mahamid, J. *et al.* Mapping amorphous calcium phosphate transformation into crystalline mineral from the cell to the bone in zebrafish fin rays. *Proc Natl Acad Sci U S A* **107**, 6316-6321 (2010).

14. Niu, L.N. *et al.* Collagen intrafibrillar mineralization as a result of the balance between osmotic equilibrium and electroneutrality. *Nat Mater* **16**, 370-378 (2017).

15. Kim, D., Lee, B., Thomopoulos, S. & Jun, Y.S. The role of confined collagen geometry in decreasing nucleation energy barriers to intrafibrillar mineralization. *Nat Commun* **9**, 962 (2018).

16. Reznikov, N., Bilton, M., Lari, L., Stevens, M.M. & Kroger, R. Fractal-like hierarchical organization of bone begins at the nanoscale. *Science* **360** (2018).

17. Gupta, H.S., Seto, J., Wagermaier, W., Zaslansky, P., Boesecke, P. & Fratzl, P. Cooperative deformation of mineral and collagen in bone at the nanoscale. *Proc Natl Acad Sci U S A* **103**, 17741-17746 (2006).

18. Rodriguez, D.E. *et al.* Multifunctional role of osteopontin in directing intrafibrillar mineralization of collagen and activation of osteoclasts. *Acta Biomater* **10**, 494-507 (2014).

19. Zhu, L., Luo, D. & Liu, Y. Effect of the nano/microscale structure of biomaterial scaffolds on bone regeneration. *Int J Oral Sci* **12**, 6 (2020).

20. Grunewald, T.A. *et al.* Mapping the 3D orientation of nanocrystals and nanostructures in human bone: Indications of novel structural features. *Sci Adv* **6**, eaba4171 (2020).

21. Wang, L., You, X., Zhang, L., Zhang, C. & Zou, W. Mechanical regulation of bone remodeling. *Bone Res* **10**, 16 (2022).

22. Thi, M.M., Suadicani, S.O., Schaffler, M.B., Weinbaum, S. & Spray, D.C. Mechanosensory responses of osteocytes to physiological forces occur along processes and not cell body and require alphaVbeta3 integrin. *Proc Natl Acad Sci U S A* **110**, 21012-21017 (2013).

23. Dupont, S. *et al.* Role of YAP/TAZ in mechanotransduction. *Nature* **474**, 179-183 (2011).

24. Wang, L., You, X., Lotinun, S., Zhang, L., Wu, N. & Zou, W. Mechanical sensing protein PIEZO1 regulates bone homeostasis via osteoblast-osteoclast crosstalk. *Nat Commun* **11**, 282 (2020).

25. Youlten, S.E. *et al.* Osteocyte transcriptome mapping identifies a molecular landscape controlling skeletal homeostasis and susceptibility to skeletal disease. *Nat Commun* **12**, 2444 (2021).

26. McHugh, J. Osteocyte death promotes bone loss. *Nat Rev Rheumatol* **16**, 539 (2020).

27. Wilson, C. Osteocytes, RANKL and bone loss. *Nat Rev Endocrinol* **7**, 693 (2011).

28. Shi, T. *et al.* Osteocyte-derived sclerostin impairs cognitive function during ageing and Alzheimer's disease progression. *Nat Metab* **6**, 531-549 (2024).

29. Owen, R. & Reilly, G.C. In vitro Models of Bone Remodelling and Associated Disorders. *Front Bioeng Biotechnol* **6**, 134 (2018).

30. Park, Y., Sato, T. & Lee, J. Functional and analytical recapitulation of osteoclast biology on demineralized bone paper. *Nat Commun* **14**, 8092 (2023).

31. Ren, X. *et al.* Osteoprotegerin reduces osteoclast resorption activity without affecting osteogenesis on nanoparticulate mineralized collagen scaffolds. *Sci Adv* **5**, eaaw4991 (2019).

32. Costa, D.O. *et al.* The differential regulation of osteoblast and osteoclast activity by surface topography of hydroxyapatite coatings. *Biomaterials* **34**, 7215-7226 (2013).

33. Duarte, J.H. Rheumatoid arthritis: Osteoclasts and ACPAs--the joint link. *Nat Rev Rheumatol* **12**, 69 (2016).

34. Ueki, Y. *et al.* Increased myeloid cell responses to M-CSF and RANKL cause bone loss and inflammation in SH3BP2 "cherubism" mice. *Cell* **128**, 71-83 (2007).

35. Kim, M.K., Paek, K., Woo, S.M. & Kim, J.A. Bone-on-a-Chip: Biomimetic Models Based on Microfluidic Technologies for Biomedical Applications. *ACS Biomater Sci Eng* **9**, 3058-3073 (2023).

36. Phillips, R. Progress toward 'bone-on-a-chip'. *Nat Rev Rheumatol* **19**, 463 (2023).

37. Wang, J.S. *et al.* Control of osteocyte dendrite formation by Sp7 and its target gene osteocrin. *Nat Commun* **12**, 6271 (2021).

38. Thrivikraman, G. *et al.* Rapid fabrication of vascularized and innervated cell-laden bone models with biomimetic intrafibrillar collagen mineralization. *Nat Commun* **10**, 3520 (2019).

39. Subbiah, R. *et al.* Engineering of an Osteoinductive and Growth Factor-Free Injectable Bone-Like Microgel for Bone Regeneration. *Adv Healthc Mater* **12**, e2200976 (2023).

40. Boskey, A. & Pleshko Camacho, N. FT-IR imaging of native and tissue-engineered bone and cartilage. *Biomaterials* **28**, 2465-2478 (2007).

41. Dallas, S.L. & Bonewald, L.F. Dynamics of the transition from osteoblast to osteocyte. *Ann N Y Acad Sci* **1192**, 437-443 (2010).

42. Qin, L., Liu, W., Cao, H. & Xiao, G. Molecular mechanosensors in osteocytes. *Bone Res* **8**, 23 (2020).

43. Diegel, C.R. *et al.* Inhibiting WNT secretion reduces high bone mass caused by Sost loss-of-function or gain-of-function mutations in Lrp5. *Bone Res* **11**, 47 (2023).

44. He, J. *et al.* Dissecting human embryonic skeletal stem cell ontogeny by single-cell transcriptomic and functional analyses. *Cell Res* **31**, 742-757 (2021).

45. Zhang, X. *et al.* Divide-and-conquer strategy with engineered ossification center organoids for rapid bone healing through developmental cell recruitment. *Nat Commun* **16**, 6200 (2025).

46. Delgado-Calle, J. & Bellido, T. The osteocyte as a signaling cell. *Physiol Rev* **102**, 379-410 (2022).

47. Xiong, J., Piemontese, M., Thostenson, J.D., Weinstein, R.S., Manolagas, S.C. & O'Brien, C.A. Osteocyte-derived RANKL is a critical mediator of the increased bone resorption caused by dietary calcium deficiency. *Bone* **66**, 146-154 (2014).

48. Wang, X., Ji, L., Wang, J. & Liu, C. Matrix stiffness regulates osteoclast fate through integrin-dependent mechanotransduction. *Bioact Mater* **27**, 138-153 (2023).

49. Glantschnig, H., Fisher, J.E., Wesolowski, G., Rodan, G.A. & Reszka, A.A. M-CSF, TNFalpha and RANK ligand promote osteoclast survival by signaling through mTOR/S6 kinase. *Cell Death Differ* **10**, 1165-1177 (2003).

50. Stegen, S. *et al.* Osteocytic oxygen sensing controls bone mass through epigenetic regulation of sclerostin. *Nat Commun* **9**, 2557 (2018).

51. Wei, Z. *et al.* Osteostaticytes: A novel osteoclast subset couples bone resorption and bone formation. *J Orthop Translat* **47**, 144-160 (2024).

52. Mun, S.H., Park, P.S.U. & Park-Min, K.H. The M-CSF receptor in osteoclasts and beyond. *Exp Mol Med* **52**, 1239-1254 (2020).

53. Curtis, J.R. *et al.* Comparative effectiveness of denosumab vs alendronate among postmenopausal women with osteoporosis. *J Bone Miner Res* **39**, 826-834 (2024).

54. Fitzpatrick, D., Lannon, R. & McCarroll, K. Postmenopausal Osteoporosis. *N Engl J Med* **390**, 675 (2024).

55. Fisher, J.E. *et al.* Alendronate mechanism of action: geranylgeraniol, an intermediate in the mevalonate pathway, prevents inhibition of osteoclast formation, bone resorption, and kinase activation in vitro. *Proc Natl Acad Sci U S A* **96**, 133-138 (1999).

56. Park, J. *et al.* CCL28-induced RARbeta expression inhibits oral squamous cell carcinoma bone invasion. *J Clin Invest* **129**, 5381-5399 (2019).

57. Mansoorifar, A., Gordon, R., Bergan, R. & Bertassoni, L.E. Bone-on-a-chip: microfluidic technologies and microphysiologic models of bone tissue. *Adv Funct Mater* **31** (2021).

58. Sun, W. *et al.* Neuro-bone tissue engineering: emerging mechanisms, potential strategies, and current challenges. *Bone Res* **11**, 65 (2023).

59. Staines, K.A. *et al.* Hypomorphic conditional deletion of E11/Podoplanin reveals a role in osteocyte dendrite elongation. *J Cell Physiol* **232**, 3006-3019 (2017).

60. Weivoda, M.M. *et al.* Identification of osteoclast-osteoblast coupling factors in humans reveals links between bone and energy metabolism. *Nat Commun* **11**, 87 (2020).

61. Tiskratok, W., Yamada, M., Watanabe, J., Pengyu, Q., Kimura, T. & Egusa, H. Mechanoregulation of Osteoclastogenesis-Inducing Potentials of Fibrosarcoma Cell Line by Substrate Stiffness. *Int J Mol Sci* **24** (2023).

62. Takegahara, N., Kim, H. & Choi, Y. Unraveling the intricacies of osteoclast differentiation and maturation: insight into novel therapeutic strategies for bone-destructive diseases. *Exp Mol Med* **56**, 264-272 (2024).

63. Kim, H.J., Kang, W.Y., Seong, S.J., Kim, S.Y., Lim, M.S. & Yoon, Y.R. Follistatin-like 1 promotes osteoclast formation via RANKL-mediated NF-kappaB activation and M-CSF-induced precursor proliferation. *Cell Signal* **28**, 1137-1144 (2016).

64. Alshbool, F.Z. & Mohan, S. Emerging multifunctional roles of Claudin tight junction proteins in bone. *Endocrinology* **155**, 2363-2376 (2014).

65. Choi, S.J., Han, J.H. & Roodman, G.D. ADAM8: a novel osteoclast stimulating factor. *J Bone Miner Res* **16**, 814-822 (2001).

66. Xu, H. *et al.* Targeting strategies for bone diseases: signaling pathways and clinical studies. *Signal Transduct Target Ther* **8**, 202 (2023).

67. Plotkin, L.I., Weinstein, R.S., Parfitt, A.M., Roberson, P.K., Manolagas, S.C. & Bellido, T. Prevention of osteocyte and osteoblast apoptosis by bisphosphonates and calcitonin. *J Clin Invest* **104**, 1363-1374 (1999).

68. El-Masri, B.M. *et al.* Mapping RANKL- and OPG-expressing cells in bone tissue: the bone surface cells as activators of osteoclastogenesis and promoters of the denosumab rebound effect. *Bone Res* **12**, 62 (2024).

69. Fu, Q. *et al.* Reduced osteoprotegerin expression by osteocytes may contribute to rebound resorption after denosumab discontinuation. *JCI Insight* **8** (2023).

70. Jin, W. *et al.* Engineered osteoclasts as living treatment materials for heterotopic ossification therapy. *Nat Commun* **12**, 6327 (2021).

71. Gu, C. *et al.* Targeting initial tumour-osteoclast spatiotemporal interaction to prevent bone metastasis. *Nat Nanotechnol* **19**, 1044-1054 (2024).

72. Jackett, K.N., Browne, A.T., Aber, E.R., Clements, M. & Kaplan, R.N. How the bone microenvironment shapes the pre-metastatic niche and metastasis. *Nat Cancer* **5**, 1800-1814 (2024).

73. Gormley, M., Creaney, G., Schache, A., Ingarfield, K. & Conway, D.I. Reviewing the epidemiology of head and neck cancer: definitions, trends and risk factors. *Br Dent J* **233**, 780-786 (2022).

74. Chow, L.Q.M. Head and Neck Cancer. *N Engl J Med* **382**, 60-72 (2020).

75. Elmusrati, A.A., Pilborough, A.E., Khurram, S.A. & Lambert, D.W. Cancer-associated fibroblasts promote bone invasion in oral squamous cell carcinoma. *Br J Cancer* **117**, 867-875 (2017).

76. Nakamura, K. *et al.* The periosteum provides a stromal defence against cancer invasion into the bone. *Nature* **634**, 474-481 (2024).

77. Choi, S. *et al.* Bone-matrix mineralization dampens integrin-mediated mechanosignalling and metastatic progression in breast cancer. *Nat Biomed Eng* **7**, 1455-1472 (2023).

78. Liu, F. *et al.* Single-cell profiling of bone metastasis ecosystems from multiple cancer types reveals convergent and divergent mechanisms of bone colonization. *Cell Genom*, 100888 (2025).

79. Mandal, M. *et al.* Epithelial to mesenchymal transition in head and neck squamous carcinoma: association of Src activation with E-cadherin down-regulation, vimentin expression, and aggressive tumor features. *Cancer* **112**, 2088-2100 (2008).

80. Wei, S.C. *et al.* Matrix stiffness drives epithelial-mesenchymal transition and tumour metastasis through a TWIST1-G3BP2 mechanotransduction pathway. *Nat Cell Biol* **17**, 678-688 (2015).

81. Kfoury, Y. *et al.* Human prostate cancer bone metastases have an actionable immunosuppressive microenvironment. *Cancer Cell* **39**, 1464-1478 e1468 (2021).

82. Schindelin, J. *et al.* Fiji: an open-source platform for biological-image analysis. *Nat Methods* **9**, 676-682 (2012).